Opto-Electronic Advances

Original Article
2020, Vol. 3, No. 1

DOI: 10.29026/oea.2020.190027

Direct laser interference patterning of nonvolatile magnetic nanostructures in $Fe_{60}Al_{40}$ alloy via disorder-induced ferromagnetism

Philipp Graus[1]*, Thomas B. Möller[1], Paul Leiderer[1], Johannes Boneberg[1] and Nikolay I. Polushkin[2]*

Current magnetic memories are based on writing and reading out the domains with opposite orientation of the magnetization vector. Alternatively, information can be encoded in regions with a different value of the saturation magnetization. The latter approach can be realized in principle with chemical order-disorder transitions in intermetallic alloys. Here, we study such transformations in a thin-film (35 nm) $Fe_{60}Al_{40}$ alloy and demonstrate the formation of periodic magnetic nanostructures (PMNS) on its surface by direct laser interference patterning (DLIP). These PMNS are nonvolatile and detectable by magnetic force microscopy (MFM) at room temperature after DLIP with a single nanosecond pulse. We provide different arguments that the PMNS we observe originate from increasing magnetization in maxima of the interference pattern because of chemical disordering in the atomic lattice of the alloy at temperatures T higher than the critical temperature T_c for the order (B2)–disorder (A2) transition. Theoretically, our simulations of the temporal evolution of a partially ordered state at $T>T_c$ reveal that the disordering rate is significant even below the melting threshold. Experimentally, we find that the PMNS are erasable with standard thermal annealing at $T<T_c$.

Keywords: thin films; laser patterning; magnetic dots; magnetic memory

Graus P, Möller T B, Leiderer P, Boneberg J, Polushkin N I. Direct laser interference patterning of nonvolatile magnetic nanostructures in $Fe_{60}Al_{40}$ alloy via disorder-induced ferromagnetism. *Opto-Electron Adv* **3**, 190027 (2020).

Introduction

Chemical order-disorder transformations in intermetallic alloys[1–10] such as Fe_xAl_{100-x} and their effects on the physical properties[11–25] attracted steady interest through decades. In particular, the phenomenon of disorder-induced ferromagnetism[11–20] was extensively studied by employing various kinds of treatments that effectively induced the structural transitions from the chemically ordered (B2) to disordered (A2) state. The performed experiments were supported by theoretical studies[21–24] that pointed out the enhancement of magnetic moments in the Fe_xAl_{100-x} (50 at.% $<x<$75 at.%) under the transformation from the B2 to A2 state.

Therefore, the question arises whether the chemically disordered state can survive upon cooling the alloy to temperatures T below the critical temperature T_c for the A2↔B2 transition[18,20]. This issue is especially relevant at the nanoscale, when precipitates of a new phase can be still smaller than the critical nucleus for the phase transformation. At a macroscopic scale, writing of nonvolatile ferromagnetism was experimentally demonstrated with $Fe_{60}Al_{40}$ thin-film specimens under their irradiation by short-pulse laser beam[18]. The goal of our study is to produce small nonvolatile magnetic structures[19,20] by focusing laser irradiation on the sample surface. In these experiments we employed direct laser interference patterning (DLIP) which allows for fabrication of large-area (up

[1]Department of Physics, University of Konstanz, 78457 Konstanz, Germany. [2]Institute for Physics of Microstructures of RAS, 603950 GSP-105 Nizhny Novgorod, Russian.
*Correspondence: P Graus, E-mail: philipp.graus@uni-konstanz.de; N I Polushkin, E-mail: nip@ipmras.ru
Received: 24 July 2019; Accepted: 4 October 2019; Published: 20 January 2020

© 2020 Institute of Optics and Electronics, Chinese Academy of Sciences. All rights reserved.

to ~1 cm^2) regular structures with periodicities down to $\lambda/2$ (λ~500 nm is laser irradiation wavelength)[26–31]. The main result we report in this article is demonstration of periodic magnetic nanostructures (PMNS) produced by DLIP. These PMNS are nonvolatile and their formation is associated with laser-induced localized chemical disordering in the alloy. We find that the formed PMNS are clearly detectable with magnetic force microscopy (MFM) at room temperature. Analyzing these findings in terms of chemical order-disorder transitions, we compare the experimental data with our simulations of the disordering/reordering rates. These studies can be useful in a view of a magnetic memory technology which would encode information in regions with different values of the magnetization saturation[18,32]. Such an approach would be an alternative to current magnetic memory technology where information bits are domains with opposite orientation of the magnetization vector.

Methods

Polycrystalline $Fe_{60}Al_{40}$ films with a thickness of ~35 nm were sputtered on (100) Si wafers covered by a natural SiO_2 layer from a target of the same composition. For sputtering, the vacuum chamber was pumped out up to a pressure of residual gas of about 10^{-9} Pa. The produced samples were post-annealed at 770 K in a vacuum furnace for times ~10^3 s and then slowly cooled. After such a treatment, the samples did not have a detectable magnetic response at room temperatures[18]. It was also shown with X-ray diffraction[18] that the annealed films were structurally ordered and that the average diameter of crystalline grains in them was about L=15 nm.

In our DLIP experiments, we used nanosecond laser pulses from an injection-seeded Nd:YAG laser (continuum powerlite 9010, λ=532 nm, τ_p=12 ns with a spot in diameter of approximately 0.6 cm on the sample surface). The laser pulse with Gaussian beam profile was split into four beams of the same TE polarization and equal intensity in all beams that impinged on the sample surface at the same angle θ, while the azimuthal angles of the incident beams were $\varphi_i=\pi(i-1)/2$ (i=1, 2, 3, 4). These beams interfered with each other to yield a two-dimensional pattern of ideally square symmetry with periodicity of $\Lambda=\lambda/(2\sin\theta)$[33]. Figure 1(a, b) shows (a) DLIP geometry and (b) simulated distribution of the light intensity, where yellow and blue colors depict regions of the highest and lowest light intensity, respectively.

The surface of patterned samples was examined with a high-resolution HR-MFM-ML3 probe (Team Nanotec) used basically for MFM. For MFM characterization, we employed a Bruker MultiMode atomic force microscope (AFM) which operated in the tapping/lift mode. Before taking MFM scans, a 0.5 T external magnetic field oriented in the film plane was applied to the sample.

The temperature calculations were performed with a 35-nm-thick $Fe_{60}Al_{40}$ film on a Si substrate, whose front

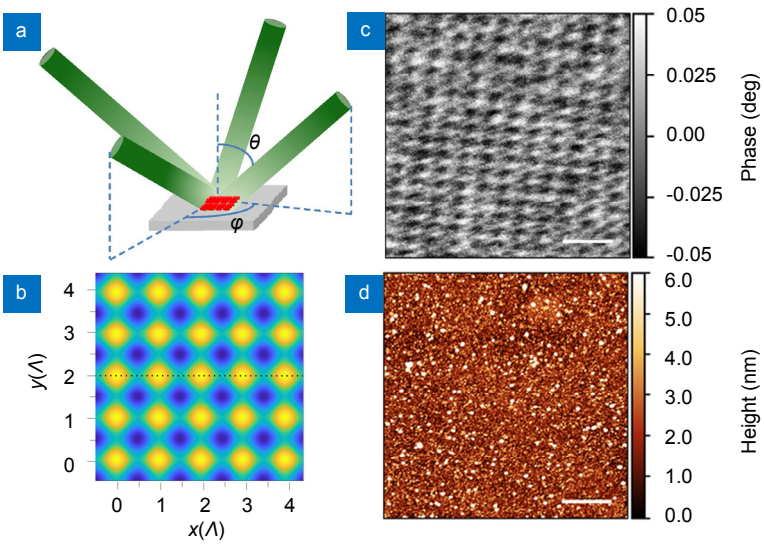

Fig. 1 | (**a**) Schematic of the DLIP geometry with four laser beams that impinge on the sample surface and their superposition provides the interference pattern. (**b**) Laser intensity distribution simulated for all the beams of TE polarization and equal intensity, which incident at the same angle θ, while the azimuthal angles are $\varphi_i=\pi(i-1)/2$, where i=1, 2, 3, 4. Under such parameters, the lattice periodicity is given by $\Lambda=\lambda/(2\sin\theta)$[33]. In our experiments, Λ was varied between 0.4 and 2.3 μm. (**c**) MFM image of a $Fe_{60}Al_{40}$ 35 nm thick sample treated by DLIP with Λ=0.4 μm and (**d**) corresponding topography.

© 2020 Institute of Optics and Electronics, Chinese Academy of Sciences. All rights reserved.

surface is irradiated by a laser (λ=532 nm) pulse with Gaussian shape and a duration of τ_p=12 ns at the full width at half maximum (FWHM). The temporal evolution of the temperature in the film was retrieved by a finite element heat flow calculations (COMSOL Multiphysics). Effects of melting and resolidification[18,20] were not taken into account. The temperature-dependent material constants for Si were taken from the COMSOL Multiphysics Material Library. For the $Fe_{60}Al_{40}$/Si interfacial thermal conductance with G=9.4×10^7 W/(m^2·K) is used[34]. As for the parameters of the $Fe_{60}Al_{40}$ film, we assume that its thermal conductivity, density, and heat capacity are k=20 W/(m·K)[35], ρ=6.5 g/cm^3 [36], and C=0.7 J/(g·K)[37], respectively.

Results

We find that a single-pulse DLIP treatment provides the formation of the PMNS which consists of alternating bright and dark spots in the MFM images. These patterns are clearly detectable down to an interference pattern periodicity of Λ=0.4 μm (Fig. 1(c)). The periodicity of the magnetic pattern in Fig. 1(c) can be determined in accordance with the distance between adjacent bright or dark spots in the MFM image. Because of the film roughness it is difficult to recognize laser-induced changes in the film topography (Fig. 1(d)).

We remark that the range of laser fluences F which provides the PMNS formation shown in Fig. 1(c) is rather narrow, $\pm 0.2F^*$ around F^*=0.18 J/cm^2. Magnetic modifications were not detected after DLIP with $F<0.8F^*$, while we observed strongly irregular magnetic patterns at $F>1.2F^*$.

We could get a regular and interpretable magnetic pattern more easily by increasing the pattern periodicity from Λ=0.4 μm (Fig. 1(c) or Fig. 2(a)) to larger values, Λ=0.6 μm (Fig. 2(b)) and Λ=2.3 μm (Fig. 2(c)). In PMNS with larger periodicities (Fig. 2(c)), one observes well-separated regions (if Λ>1.0 μm) of nonzero MFM response, and each such a region contains sub-regions with positive (bright spot) and negative (dark spot) MFM response. One can evaluate the lateral dimensions of these regions that look elongated with the aspect ratio of ≈1:2. It was previously demonstrated[38–40] by numerical simulations of the MFM response and experimentally observed in small magnetic elements that the two-contrast entities in Fig. 2(c) can be attributed to single-domain magnets, whose north and south poles generate stray fields which act on the cantilever by changing both the phase and amplitude of its vibrations. We note, however, that a single domain is not the ground state even for elongated particles which have large enough dimensions[41]. The single-domain state we observe in our patterns can result from distortion of the ground magnetization distribution by stray fields of the MFM probe[42].

It is also interesting that analyzing the correspondences between the topographical relief (Fig. 3(a)) and the MFM image (Fig. 3(b)) allows us to identify the surface features induced by the laser pulse. We see that the topographic peaks are located in those places where the MFM response is neutral between the poles of the patterned entities. Another fact is that the whole area, inside of which the MFM response is nonzero, is significantly larger (~300 nm) than that of the laser-induced bumps in the topographical relief (~100 nm). Presumably, the detected surface features result from local thickening of the film, which is associated with a change in the atomic density of the quenched material of the film after its melting[43]. It is also highly likely that the magnetic modifications occupy the areas which are much bigger than those of the melted zones within maxima of light intensity.

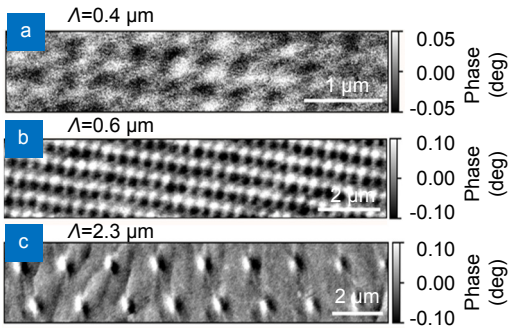

Fig. 2 | MFM images of patterned structures that have different periodicities *Λ* of the interference pattern. (**a**) 0.4 μm, (**b**), 0.6 μm, and (**c**) 2.3 μm.

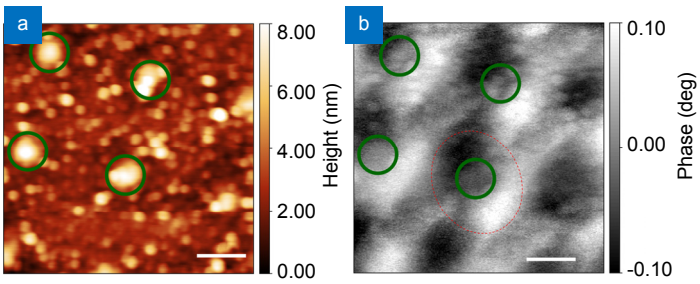

Fig. 3 | Correspondence between the laser-induced topographical relief (a) and MFM response (b). The bumps on the $Fe_{60}Al_{40}$ surface, occurring within maxima of light intensity (solid contours), are significantly smaller in their lateral dimensions than the regions in which the MFM response is nonzero. One of the patterned magnetic entities is indicated by dashed contour.

© 2020 Institute of Optics and Electronics, Chinese Academy of Sciences. All rights reserved.

Discussion

Disorder-induced ferromagnetism

We now argue that magnetization in the $Fe_{60}Al_{40}$ thin-film alloy we study can be enhanced upon its chemical disordering. Initially, the phenomenon of disorder-induced ferromagnetism was observed under plastic deformation in bulk alloys, e.g., Ref.[11,14]. In the context of our study, it is important to note that different kinds of irradiation such as high-energy ion[17] and short-pulse laser[18–20] beams can be employed for producing the ferromagnetic order via destroying the B2 superstructure in thin-film specimens.

Figure 4(a) illustrates how the B2 state is destroyed via atomic diffusion jumps through vacancies (boxes) in the Fe_xAl_{100-x} lattice where x~50 at.%. As a result, magnetic Fe atoms appear in the centers of the Fe-based unit cells (antisite defects) instead of Al atoms. This reconfiguration leads to percolation between adjacent Fe planes, thus yielding the transformation from the superparamagnetic to ferromagnetic state[11,15]. Note that the appearance of the antisite defects results in shortening the minimal distance between Fe atoms from a to $a\sqrt{3}/2$, where a is the atomic lattice constant. Qualitatively, this leads to the enhancement of exhange interactions because of the bigger overlap of d-orbitals between Fe neighbors. Figure 4(b) illustrates the calculation results performed at x=50 at. % and x=75 at. %[21], which indicate the enhancement of the magnetic moment per Fe atom (μ_{Fe}) upon the transformation from the B2 to A2 state. Based on a linear interpolation, we conclude that μ_{Fe} in the B2 and A2 state at x=60 at. % is respectively 0.8 μ_B and 1.8 μ_B.

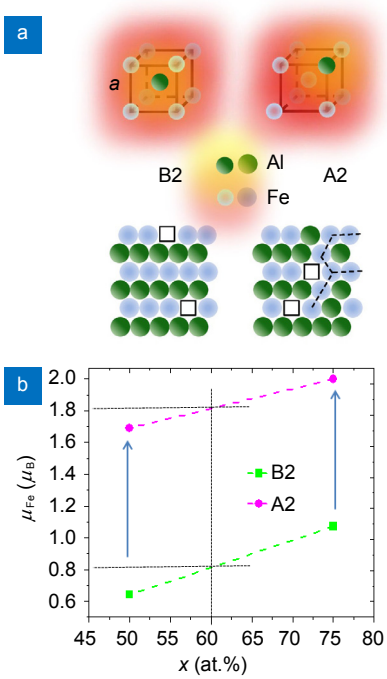

Fig. 4 | (a) Fe-based unit cells (top) and the (100) projections (bottom) of the atomic structure in the chemically ordered B2 and disordered A2 states of the Fe_xAl_{100-x} (x~50 at.%) alloy. The open boxes are vacancies in the lattice through which the atomic jumps occur for relaxation of the system to its thermodynamic equilibrium. In the A2 state there are magnetic percolation paths (dashed lines). (**b**) Simulated change of magnetic moments in Fe under the transformation from the B2 to A2 state[21].

Laser-induced disordering and reordering.

We now present our analysis of how the superstructure (B2 state) is destroyed in Fe_xAl_{100-x} alloys by rasing T above T_c, which is driven by nanosecond laser irradiation. The question is how the disordered (A2) state (and thus ferromagnetism) can be trapped upon cooling the sample below T_c. First of all, we note that laser fluences, which provide the PMNS (Figs. 1–3), are not only sufficient for temperature elevation in the maxima of light intensity significantly above T_c=1563 K[44], but even above the melting point T_m=1662 K[44]. This conclusion is based on our experimental observations of the bumps formed in the maxima of light intensity (Fig. 3(a))[43] and is supported by our calculations of temperature elevation induced by laser irradiation. In order to evaluate the temperature rise, we had to get the relationship between the incident and absorbed fluence by measuring the optical reflectivity of our samples (R=0.6) in the continuous-wave mode.

Figure 5(a–c) shows (a) the distribution of the absorbed fluence F_{abs} in units of $(1-R)F^*$ along the dashed horizontal line in Fig. 1(b) and (b) $T(t)$ dependencies at different locations through (c) a pattern of square symmetry with Λ=0.4 μm. The specific locations, inside of which we calculate $T(t)$, are as follows: 1) Maxima of light intensity [bumps (Fig. 3(a))], 2) The regions which are located outside the melted zones but in which the maximal temperature T_{max} exceeds T_c, and 3) Local minima of laser intensity along the dashed horizontal line in Fig. 1(b).

The origin of PMNS shown in Figs. 1–3 can be associated with chemical disordering in the $Fe_{60}Al_{40}$ atomic lattice at $T>T_c$. Based on theoretical considerations given in Supplementary Information, we calculate the disordering rates, which depend on the non-equlibrium concentration of vacancies generated by laser. As we do not take into account effects of melting

© 2020 Institute of Optics and Electronics, Chinese Academy of Sciences. All rights reserved.

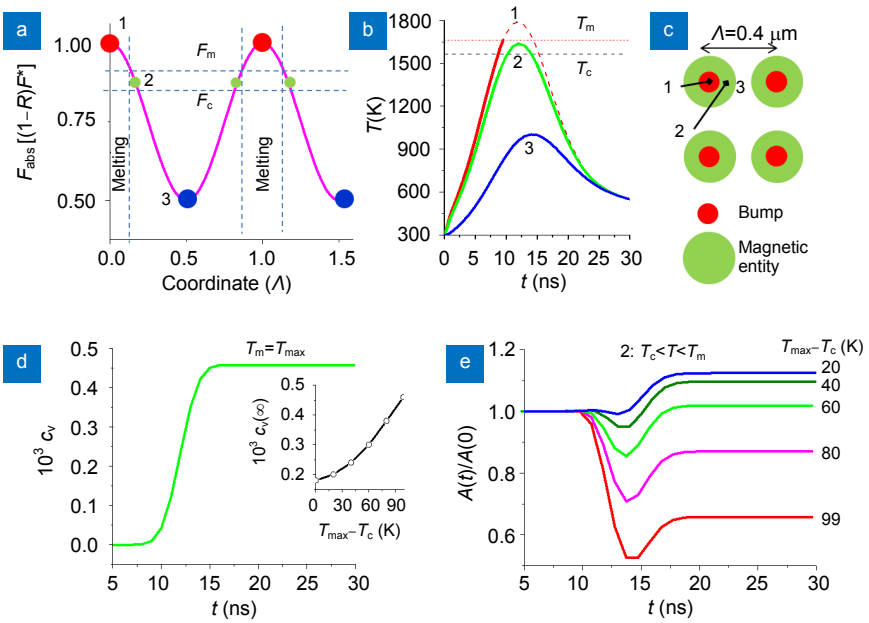

Fig. 5 | (**a**) Absorbed fluence F_{abs} as a function of coordinate along the dashed horizontal line in Fig. 1(b) with indications of different positions: 1. maxima of light intensity, where $F_{abs}=(1-R)F^*>F_m$ (F_m is the absorbed fluence required for raising the temperature up to the melting point T_m); 2. locations outside the melted zones, in which $F_c<F_{abs}<F_m$ (F_c is the absorbed fluence required for raising the temperature up to T_c); 3. local minima of light intensity. (**b**) $T(t)$ dependencies calculated in positions 1, 2, and 3, where the absorbed fluence is respectively F_{abs}=70 mJ/cm^2, F_{abs}=65 mJ/cm^2, and F_{abs}=35 mJ/cm^2. As temperature elevation was calculated with no taking into account effects of melting and resolidification[18,20], the $T(t)$ dependence calculated at $F_{abs}>F_m$ is shown by the dashed curve for $t>t_m$, where t_m is the moment of time at which the temperature rise reaches T_m. (**c**) Unit cell of the interference pattern with the marks for positions in which the $T(t)$ dependences plotted in (b) are simulated. (**d**) Non-equilibrium vacancy concentration c_v versus t in zone(s) 2 at $T_{max}=T_m$. The inset shows the asymptotic value $c_v(\infty)$ at different temperature elevations $T_{max}-T_c$ up to $T_{max}=T_m$. (**e**) Concentration wave (superstructure) amplitude $A(t)/A(0)$ as a function of time t in zone(s) 2 at different temperature elevations $T_{max}-T_c$ up to $T_{max}=T_m$.

and resolidification[18,20] in our calculations of $T(t)$ (Fig. 5(b)), we can account for the disordering rates only if $T_{max}<T_m$. Obviously, we should perform these calculations in zones where $T_c<T_{max}<T_m$, i.e., in zone(s) 2, as indicated in Fig. 5(a–c). Figure 5(d, e) shows (d) the vacancy concentration $c_v(t)$ as a function of time t and (e) changes in the concentration wave amplitude $A(t)/A(0)$ for different temperature elevations in zone(s) 2 up to $T_{max}=T_m$. As seen from Fig. 5(e), chemical disordering, i.e., decrease of $A(t)/A(0)$, becomes dominating at $T_{max}-T_c>60$ K. At lower temperature elevations above T_c, the disordering occurring at $T>T_c$ has a lower rate than the reordering does, which occurs at $T<T_c$. Therefore, erasing of the ferromagnetism in the $Fe_{60}Al_{40}$ is feasible with a train of laser pulses[20]. The concentration wave amplitude $A[T(t)]$ was found in accordance with the following equation:

$$A[T(t)]=A(0)\exp[\int_{t_1}^{t_2}\alpha(t)\mathrm{d}t] \quad , \qquad (1)$$

where $$\alpha(t)=\frac{32D(t)[(T_c-T(t)]c_v(t)}{T(t)a^2(1-x)} \quad ,$$

$D(t)=D_0\exp(-E_m/k_BT)$ is the diffusion coefficient, D_0 the pre-exponential factor, E_m the activation energy for the atomic diffusion (or enthalpy of vacancy migration), and t_1, t_2 are the starting and finishing moments of a relaxation process; see Supplementary Information. The non-equilibrium vacancy concentration shown in Fig. 5(d) is retrievable from the relaxation equation of the Bloch type

$$\frac{\mathrm{d}c_v}{\mathrm{d}t}=\frac{c_{eq}(T)-c_v}{\tau} \quad , \qquad (2)$$

where $c_{eq}(T)=\exp(-E_v/k_BT)$ is the equilibrium vacancy concentration, E_v the enthalpy of vacancy formation, $\tau=L^2/D$ the relaxation time, which is the characteristic time of vacancy life between its formation and annihilation at crystallite boundaries; see also Supplementary Information. In order to account for $A(t)$ (Fig. 5(e)), we have chosen the following parameters: $D_0=2.6\times10^{-3}$ m^2/s[7,8], E_v=0.9 eV and E_m=1.7 eV[8,9], and L=15 nm[18].

As follows from our considerations above, a long enough thermal treatment at $T<T_c$ should provide extensive formation of the B2 phase and thus reducing the magnetization[17]. It was shown previously[18] with Kerr magnetometry that the magnetic response of the $Fe_{60}Al_{40}$ alloy after its irradiation by nanosecond laser becomes comparable to that of a ferromagnetic material like Fe.

© 2020 Institute of Optics and Electronics, Chinese Academy of Sciences. All rights reserved.

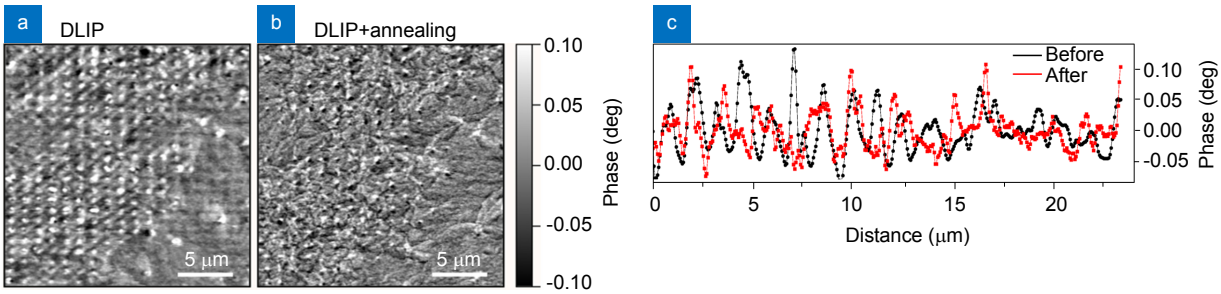

Fig. 6 | MFM images of the patterned $Fe_{60}Al_{40}$ surface at the edge of the irradiated zone. The images were taken (**a**) before and (**b**) after thermal annealing in a furnace at *T*=770 K for one hour. (**c**) Cross section of the MFM image before and after thermal annealing.

However, such a strong response practically vanishes after standard thermal annealing of the sample at T=770 K for times t~10^3 s. In our work, we used the same kind of treatment to test our explanations for the PMNS origin. Figure 6 shows MFM images of a $Fe_{60}Al_{40}$ sample (a) after DLIP at the very edge of the irradiated zone and (b) after thermal annealing of this sample. We see that the PMNS becomes much less pronounced after annealing. It is seen from the cross sections (Fig. 6(c)) of the MFM images that the degradation of the MFM pattern occurs via rather a decrease of the MFM response but not via shrinking the patterned entities. Such a behavior can be explained in terms of homogeneous nucleation of the B2 phase[6], which occurs inside the chemically disordered regions of the magnetic A2 phase.

Conclusions

Using magnetic force microscopy (MFM), we have studied the conditions for the formation of periodic magnetic nanostructures (PMNS) in the $Fe_{60}Al_{40}$ alloy under direct laser interference patterning (DLIP). The PMNS formation is associated with the effect of chemical-disorder-induced ferromagnetism when the alloy is heated in maxima of light intensity up to temperatures above the critical temperature T_c for the chemical order (B2) ↔ disorder (A2) transformation. The disordered state occurring in maxima persists in the alloy upon its cooling to temperatures below T_c, and so, these regions are nonvolatile and appear to be ferromagnetic at room temperature. As our simulations show, the disordering rate can be significant below the melting threshold at sufficient temperature elevation above T_c (Fig. 5(e)). Therefore, there can be no need to melt the film to modify the magnetism by laser in the system under study. The findings we report here are believed to have a potential for developing a magnetic memory technology[18,32] which would be alternative to current magnetic memories.

References

1. Nix F C, Shockley W. Order-disorder transformations in alloys. *Rev Mod Phys* **10**, 1–71 (1938).
2. Cook H E, de Fontaine D, Hilliard J E. A model for diffusion on cubic lattices and its application to the early stages of ordering. *Acta Metall* **17**, 765–773 (1969).
3. Metiu H, Kitahara K, Ross J. Stochastic theory of the kinetics of phase transitions. *J Chem Phys* **64**, 292–299 (1976).
4. Khachaturyan A G. Ordering in substitutional and interstitial solid solutions. *Prog Mater Sci* **22**, 1–150 (1978).
5. Martin G. Relaxation rate of conserved and nonconserved order parameters in replacive transitions. *Phys Rev B* **50**, 12362–12366 (1994).
6. Ye J, Bellon P. Nanoscale patterning of chemical order induced by displacement cascades in irradiated alloys. I. A kinetic Monte Carlo study. *Phys Rev B* **70**, 094104 (2004).
7. Mehrer H, Eggersmann M, Gude A, Salamon M, Sepiol B. Diffusion in intermetallic phases of the Fe-Al and Fe-Si Systems. *Mater Sci Eng*: *A* **239–240**, 889–898 (1997).
8. Eggersmann M, Mehrer H. Diffusion in intermetallic phases of the Fe-Al system. *Philos Mag A* **80**, 1219–1244 (2000).
9. Würschum R, Grupp C, Schaefer H E. Simultaneous study of vacancy formation and migration at high temperatures in *B*2-type Fe aluminides. *Phys Rev Lett* **75**, 97–100 (1995).
10. Stana M, Sepiol B, Kozubski R, Leitner M. Chemical ordering beyond the superstructure in long-range ordered systems. *New J Phys* **18**, 113051(2016).
11. Huffman G P, Fisher R M. Mössbauer studies of ordered and cold-worked Fe–Al alloys containing 30 to 50 at. % aluminum. *J Appl Phys* **38**, 735 (1967).
12. Beck P A. Some recent results on magnetism in alloys. *Metall Mater Trans B* **2**, 2015–2024 (1971).
13. Hernando A, Amils X, Nogués J, Surinãch S, Baró M D et al. Influence of magnetization on the reordering of nanostructured ball-milled Fe-40 at. % Al powders. *Phys Rev B* **58**, R118649(R) (1998).
14. Menéndez E, Sort J, Liedke M O, Fassbender J, Suriñach S et al. Two-fold origin of the deformation-induced ferromagnetism in bulk $Fe_{60}Al_{40}$ (at.%) alloys. *New J Phys* **10**, 103030 (2008).
15. Zamora L E, Alcázar G A P, Vélez G Y, Betancur J D, Marco J F et al. Disorder effect on the magnetic behavior of mechanically alloyed $Fe_{1-x}Al_x$ ($0.2 \le x \le 0.4$). *Phys Rev B* **79**, 094418 (2009).
16. Murakami Y, Niitsu K, Tanigaki T, Kainuma R, Park H S et al. Magnetization amplified by structural disorder within nanometre-

© 2020 Institute of Optics and Electronics, Chinese Academy of Sciences. All rights reserved.

scale interface region. *Nat Commun* **5**, 4133 (2014).
17. Bali R, Wintz S, Meutzner F, Hübner R, Boucher R et al. Printing nearly-discrete magnetic patterns using chemical disorder induced ferromagnetism. *Nano Lett* **14**, 435–441 (2014).
18. Polushkin N I, Oliveira V, Vilar R, He M, Shugaev M V et al. Phase- change magnetic memory: Rewritable ferromagnetism by laser quenching of chemical disorder in $Fe_{60}Al_{40}$ alloy. *Phys Rev Appl* **10**, 024023 (2018).
19. Yoshida Y, Oosawa K, Watanabe S, Kaiju H, Kondo K et al. Nanopatterns induced by pulsed laser irradiation on the surface of an Fe-Al alloy and their magnetic properties. *Appl Phys Lett* **102**, 183109 (2013).
20. Ehrler J, He M, Shugaev M V, Polushkin N I, Wintz S et al. Laser-rewriteable ferromagnetism at thin-film surfaces. *ACS Appl Mater Interfaces* **10**, 15232–15239 (2018).
21. Apiñaniz E, Plazaola F, Garitaonandia J S. Electronic structure calculations of Fe-rich ordered and disordered Fe-Al alloys. *Eur Phys J B* **31**, 167–177 (2003).
22. Plazaola F, Apiñaniz E, Rodriguez D M, Legarra E, Garitaonandia J S. Fe-Al alloys' magnetism. In *Advanced Magnetic Materials*, Ed. by Malkinski L, University of New Orleans, USA, 2002.
23. Kulikov N I, Postnikov A V, Borstel G, Braun J. Onset of magnetism in *B*2 transition-metal aluminides. *Phys Rev B* **59**, 6824–6833 (1999).
24. Smirnov A V, Shelton W A, Johnson D D. Importance of thermal disorder on the properties of alloys: origin of paramagnetism and structural anomalies in bcc-based $Fe_{1-x}Al_x$. *Phys Rev B* **71**, 064408 (2005).
25. Palm M, Stein F, Dehm G. Iron aluminides. *Annu Rev Mater Res* **49**, 297 – 326 (2019).
26. Müller-Meskamp L, Kim Y H, Roch T, Hofmann S, Scholz R et al. Efficiency enhancement of organic solar cells by fabricating periodic surface textures using direct laser interference patterning. *Adv Mater* **24**, 906–910 (2012).
27. Daniel C, Mücklich F, Liu Z. Periodical micro-nano-structuring of metallic surfaces by interfering laser beams. *Appl Surf Sci* **208–209**, 317–321 (2003).
28. Zheng M, Yu M, Liu Y, Skomski R, Liou S H et al. Magnetic nanodot arrays produced by direct laser interference lithography. *Appl Phys Lett* **79**, 2606–2608 (2001).
29. Stärk M, Schlickeiser F, Nissen D, Hebler B, Graus P et al. Controlling the magnetic structure of Co/Pd thin films by direct laser interference patterning. *Nanotechnology* **26**, 205302 (2015).
30. Martín-Fabiani I, Riedel S, Rueda D R, Siegel J, Boneberg J et al. Micro- and submicrostructuring thin polymer films with two and three-beam single pulse laser interference lithography. *Langmuir* **30**, 8973−8979 (2014).
31. Davies C S, Janušonis J, Kimel A V, Kirilyuk A, Tsukamoto A et al. Towards massively parallelized all-optical magnetic recording. *J Appl Phys* **123**, 213904 (2018).
32. Timmerwilke J, Liou S H, Cheng S F, Edelstein A S, Rewriting magnetic phase change memory by laser heating. *J Phys D: Appl Phys* **49**, 165005 (2016).
33. Wang D P, Wang Z B, Zhang Z A, Yue Y, Li D Y et al. Effects of polarization on four-beam laser interference lithography. *Appl Phys Lett* **102**, 081903 (2013).
34. Bischof J. Metallische dünnfilmschmelzen nach pulslaser-bestrahlung: phasenumwandlungen und Instabilitäten (Konstanz, Univ, Diss, 1997).
35. Rudajevová A, Buriánek J. Determination of thermal diffusivity and thermal conductivity of Fe-Al Alloys in the concentration range 22 to 50 at.% Al. *J Phase Equilib* **22**, 560–563 (2001).
36. Chanbi D, Ogam E, Amara S E, Fellah Z E A. Synthesis and mechanical characterization of binary and ternary intermetallic alloys based on Fe-Ti-Al by resonant ultrasound vibrational methods. *Materials* **11**, 746 (2018).
37. Piatkowski J, Przeliorz R, Jablonska M. The specific heat capacity and oxidation kinetics of NiAl, FeAl and TiAl alloys. *Solid State Phenom* **203–204**, 431–434 (2013).
38. Bukharaev A A, Ovchinnikov D V, Nurgazizov N I, Kukovitskiĭ E F, Klaĭber M et al. Investigation of micromagnetism and magnetic reversal of Ni nanoparticles using a magnetic force microscope. *Phys Solid State* **40**, 1163–1168 (1998).
39. Alekseev A M, Bykov V A, Popkov A F, Polushkin N I, Korneev V I. Observation of remanent states of small magnetic particles: Micromagnetic simulation and experiment. *J Exp Theor Phys Lett* **75**, 268–272 (2002).
40. Zhu X B, Grutter P. Magnetic force microscopy studies of patterned magnetic structures. *IEEE Trans Magn* **39**, 3420–3425 (2003).
41. Zhang W, Singh R, Bray-Ali N, Haas S. Scaling analysis and application: phase diagram of magnetic nanorings and elliptical nanoparticles. *Phys Rev B* **77**, 144428 (2008).
42. Chang J, Mironov V L, Gribkov B A, Fraerman A A, Gusev S A et al. Magnetic state control of ferromagnetic nanodots by magnetic force microscopy probe. *J Appl Phys* **100**, 104304 (2006).
43. Wei J S, Jiao X B, Gan F X, Xiao M F. Laser pulse induced bumps in chalcogenide phase change films. *J Appl Phys* **103**, 124516 (2008).
44. Stein F, Palm M. Re-determination of transition temperatures in the Fe–Al system by differential thermal analysis. *Int J Mater Res* **98**, 580–588 (2007).

Acknowledgements

N. I. Polushkin acknowledges the support by the Russian Foundation for Basic Research (grant #18-02-00827_a) and by the Program of Fundamental Research of the Presidium of the Russian Academy of Sciences "Nanostructures: Physics,Chemistry, Biology, Technology, Basics". P. Graus, T. B. Möller, P. Leiderer and J. Boneberg acknowledge the support by the DFG through the SFB 767 at the University of Konstanz.

Competing interests

The authors declare no competing financial interests.

Supplementary information

Supplementary information for this paper is available at https://doi.org/10.29026/oea.2020.190027

© 2020 Institute of Optics and Electronics, Chinese Academy of Sciences. All rights reserved.